Triggered earthquakes suppressed by an evolving stress shadow from a propagating dyke

Robert G. Green[1]

Tim Greenfield[1]

Robert S. White[1]

Corresponding Author: Green, Robert G. rgcg3@cam.ac.uk

CONTACT AUTHOR TO REQUEST AN ARTICLE PDF

[1]Bullard Laboratories, Department of Earth Sciences, University of Cambridge, Madingley Road, Cambridge,

UK, CB3 0EZ.

Small static stress increases resulting from large earthquakes may trigger aftershock earthquake swarms, while stress reductions may reduce earthquake failure rates[1,2] (stress shadowing). However, seismic waves from large earthquakes also cause transient dynamic stresses which may trigger seismicity[3,4]. This makes it difficult to separate the relative influence of static and dynamic stress changes on aftershocks. Here we present an excellent demonstration of static stress triggering and shadowing during the intrusion of a 46 km long, 5 m wide igneous dyke in central Iceland. During the emplacement, bursts of seismicity 5–15 km away from the dyke are first triggered and then abruptly switched off as the dyke tip propagated away from Bárðarbunga volcano and along the neovolcanic rift zone. We use seismicity to map the location of the dyke in the subsurface and Global Positioning System measurements to constrain its opening. We then calculate the evolving static stress changes as the dyke propagated and show that the stressing rate controls both the trigger and then suppression of earthquake rates in three areas adjacent to the dyke. Similar small static stress changes may be important in triggering seismicity near geothermal areas, deflating oil and gas fields and areas being hydrofractured to enhance hydrocarbon recovery.

It is widely reported that regions of abundant aftershocks (or advanced main shock recurrence) following large earthquakes correlate spatially with the small static stress increases produced by permanent fault displacements[1,4,5]. Dynamic stress radiation patterns have also been invoked to explain aftershock clustering[3], but dynamic triggering cannot impart a stress shadow that would reduce seismicity in response to stress decrease at a given location[6]. Many studies have suggested that in regions where the static stress is decreased, aftershocks are rare or seismicity rates are reduced as a consequence of the negative stress shadow caused by the fault rupture[1,6,7,8,9]. However, convincing observations of the stress shadowing effect have been notoriously hard to demonstrate, and some have argued that there is a lack of evidence that they exist at all[3,10,11]. The challenge has been to demonstrate convincing and significant earthquake rate drops that correlate unambiguously with a stress decrease, because a high preceding seismicity rate is required. This task relies on the correct determination of static stresses. Unfortunately, geometrical irregularities in large faults result in a complex stress field which is difficult to resolve close to an active fault, thereby hampering the detection of a sharp seismicity decline within a strong stress shadow near the source. Alternative metrics of rate counting have also suggested the absence of rate drops following large earthquakes[10]. The existence of static stress shadows has therefore remained a contentious question. Here we provide clear evidence of the stress shadow effect, with three separate regions showing unambiguous seismicity rate decreases in response to negative static stress perturbations.

On 16th August 2014 volcanic unrest began at the subglacial central volcano Bárðarbunga in Iceland,

with a surge of intense seismicity in the caldera (Figure 1). Rapidly migrating earthquakes delineated a propagating dyke, which moved first south-east radially away from the volcano, then turned a sharp corner and propagated to the north-east. Our well-constrained locations of over 30,000 earthquakes, mostly near the leading edge of the dyke, track its varying rate of segmented lateral growth[12] (see Supplementary Movie 1). Over a 10 day period the dyke propagated 46 km at an average depth of 7 km below sea level, before an effusive fissure eruption broke out at Holuhraun, 5 km north of the Vatnajökull ice cap.

As the intrusion propagated, several regions adjacent to the dyke lit up abruptly with bursts of increased seismicity. Earthquakes on the north-east flank of Bárðarbunga (region 1, Figure 1) started simultaneously with the initial south-easterly dyke tip migration, and earthquake swarms at Kistufell (region 2) and Kverkfjöll geothermal field (region 3) began soon after. These regions have all been historically seismically active[13] at low background levels, orders of magnitude smaller than the swarm levels. Regions 2 and 3 exhibited low but measurable rates in the months preceding the unrest. Earthquake rates increased fifty fold in region 2 and hundred fold in region 3 as the opening dyke caused stress increases. All three regions of seismicity subsequently terminated abruptly, each at different times. Modelling of the evolving coulomb stress perturbation from a combination of the opening dyke and a deflating source beneath Bárðarbunga caldera shows that the onset of seismicity in these regions is triggered when the stressing rate begins to increase. The subsequent shut-off of seismicity in each region correlates well with the time when the stressing rate from the propagating dyke became negative at that locality. As the dyke tip advanced past the glacier edge elevated seismicity was triggered in the Askja region further north (Figure 1) by the increasing stress. This seismicity did not subsequently shut off because the coulomb stresses remained positive ahead of the final dyke tip location.

Coulomb stress calculations rely on knowing the trigger fault geometry, the rake and the coefficient of friction, as well as correct determination of the subsurface deformation from the intrusion. We generate a time dependent deformation model of the Bárðarbunga deflation and dyke opening by integrating the earthquake locations, which constrain the daily geometry of active dyke segments, with the amount of opening determined from surface displacements at Global Positioning System (GPS) stations adjacent to the dyke[12]. The total dyke length is 46 km and opening occurs between 2–8 km below

sea level, with variable opening seen in each of the segments (Supplementary Movie 2). The largest opening of 5.1 m occurred on the segment north of the Vatnajökull ice-cap margin. The total volume of the dyke was 0.55 km³, similar to that deduced by Sigmundsson et al.[12]

Our dense local seismic network provides excellent constraints on the locations and focal mechanisms of the triggered earthquakes (Figures 1,2), even though they are small. We therefore evaluate the daily static coulomb stress changes on representative target faults with fault planes that are accurately and consistently well determined within each of the triggered regions.

As the dyke opened, lobes of positive coulomb stress emanated from the tips of the dyke segments and these migrated forwards as the dyke propagated. Increased seismicity rates in each of the swarm regions (Figures 3a,d,g) occur simultaneously with the increased stressing rate as positive stress lobes migrated into those regions. With onwards dyke propagation the positive stress lobes migrated past the swarm regions and negative stress shadows expanded into them, clamping the faults and shutting down the seismicity (Figures 3b,e,h). The seismicity shut-off coincides with a switch to a negative stressing rate (Figures 3c,f,i). The daily coulomb stress field for each region is presented in Supplementary Figures 2–4.

Timing of both the earthquake triggering and then suppression are consistent with a rate-state friction model[14] of coulomb stress transfer to a population of rate weakening faults. Seismicity rates rise when the stressing rate increases above the background level, and are shut-off when the stressing rate becomes negative (Figures 3c,f,i). Using the known background seismicity rate, and fitting for two parameters, the background stressing rate, $\dot{\tau}$, and the product of the effective normal stress and a fault constitutive parameter, Aσ, predicts a cumulative seismicity (blue lines) on Figures 3c,f,i. The excellent consistency with the observed seismicity provides support that the observed swarm seismicity is explained by the changing stressing rates.

At Kistufell the shut-off of the seismicity predicted by the rate-state model is slightly earlier than that shown by the observed earthquakes (Figure 3f). This is because our opening model is constrained by GPS solutions every 24 hours and the stress is assumed to vary linearly between the data points. However, on day 230 when the seismicity at Kistufell shuts-off, detailed inspection of the earthquake locations (Supplementary Figure 7) show that the intrusion of the dyke segment which controls whether the stress is

increasing or decreasing does not occur until 2 hours before the timestamp. This implies that the stress was actually increasing in the region of interest up to that point and the assumption of a linear stress evolution is not correct. The same late opening argument explains why western Kverkfjöll events fall on the boundary of negative stresses from that small segment (Supplementary Figure 8). Finer resolution GPS time-series would reduce this error.

The seismicity suppression we observe in response to a negative stressing rate is as near to instantaneous as can be determined from the daily resolution of the available GPS measurements. Therefore we cannot discount an instantaneous coulomb failure model[15], where faults respond instantaneously to the coulomb stress change with seismicity rate changes directly proportional to increasing stress, but zero rate for decreasing stress. In order to test whether the rate-state model is better than the instantaneous coulomb failure model, more time must elapse in order to observe the relaxation of the stress shadow and the return to background seismicity rates in the triggered regions.

Confidence in the observation of this immediate stress shadow comes from the co-location of the trigger and shadow effect. Triggering first elevates the seismicity rate, so the subsequent seismicity rate drop in the same location is seen as a clear and unambiguous halt. There is no need to de-cluster the earthquake catalogue (which removes cascading earthquake swarm sequences) to demonstrate the seismicity decline. Additionally the co-location indicates no detection bias that might favour triggered over shadow zone, as is a risk in aftershock clustering studies. Coulomb stress changes of a few tenths of a bar (a few hundred kPa) that we deduce as sufficient to trigger and influence seismicity rates are also similar to the stress changes deduced from aftershock studies[16,17]. The seismicity shut-offs occur asynchronously between the regions, suggesting that they are not an artefact caused by a change in detection sensitivity of the seismic network. In addition, over the period of this study there was no sustained volcanic tremor (which can mask signals from small earthquakes and therefore inhibit detection), and no change in the operational network. The abrupt nature of the shut-offs also suggests that the seismicity rate decreases are not due to exhaustion of earthquake nucleation sites within the fault systems.

Analysis of the seismicity rate changes caused by aseismic deformation (such as dyke intrusion) is advantageous for examining stress effects compared to studies following large earthquakes because the

aseismic deformation removes the possibility of dynamic stress triggering[18,19,20,21]. In a recent demonstration of a stress shadow from the Joshua Tree - Landers earthquake doublet[16] a small but immediate jump in seismicity before the rate decline complicates the shadow effect, but could be attributed to a dynamic triggering effect which decays away to leave the longer lasting static stress shadow. In our study the rate drop we observe is immediate, and the stress field is dominated by the evolving static stress of the aseismic dyke opening. Large earthquakes (M4+) associated with the collapse of Bárðarbunga caldera start on day 233, after the period of triggering and suppression.

Stress modelling uncertainty from receiver fault variability is reduced in this study through high quality earthquake locations and focal mechanism constraints from a dense local seismic network (Supplementary Figure 9). Fault-plane solutions have excellent coverage of the focal sphere, with a minimum of 17 and an average of 40 polarity picks. Another advantage of the co-location of the triggered and shadowed zones is that we know the faulting mechanisms that exhibited triggered activity and so understand which faults are being shut down. Therefore we can be confident that we have made the static stress computations on correctly orientated target faults. In addition, we find that varying the coefficient of friction (μ) between 0.2 and 0.6 still produces a triggered seismicity increase followed by a stress shadowing effect (Supplementary Figure 6).

As a result we conclude that this study provides a robust observation of a stress shadow effect, with a stress triggered increase of seismicity and then a decreasing static coulomb stress causing an immediate seismicity halt in three separate earthquake swarms

References (30):

1. Stein, R. S. The role of stress transfer in earthquake occurrence. *Nature* **402,** 605–609 (1999).

2. Steacy, S., Gomberg, J. & Cocco, M. Introduction to special section: Stress transfer, earthquake triggering, and time-dependent seismic hazard. *J. Geophys. Res.* **110,** B05S01 (2005).

3. Kilb, D., Gomberg, J. & Bodin, P. Triggering of earthquake aftershocks by dynamic stresses. *Nature* **408,** 570–574 (2000).

4. Harris, R. A. Introduction to special section: Stress triggers, stress shadows, and

implications for seismic hazard. *J. Geophys. Res.* **103,** 347–358 (1998).

5. Doser, D. I. & Robinson, R. Modelling stress changes induced by earthquakes in the southern Marlborough region, South Island, New Zealand. *Bull. Seismol. Soc. Am.* **92,** 3229–3238 (2002).

6. Toda, S. & Stein, R. S. Toggling of seismicity by the 1997 Kagoshima earthquake couplet: A demonstration of time-dependent stress transfer. *J. Geophys. Res.* **108,** B122527 (2003).

7. Reasenberg. P. A. & Simpson, R. W. Response of regional seismicity to the static stress change produced by the Loma Prieta Earthquake. *Science **255,*** 1687–1690 (1992).

8. Parsons, T., Stein, R. S., Simpson, R. W. & Reasenberg, P.A. Stress sensitivity of fault seismicity: A comparison between limited-offset oblique and major strike-slip faults. *J. Geophys. Res.* **104,** 183–202 (1999).

9. Segall, P. E. K., Llenos, A. L., Yun, S-H., Bradley, A. M & Syracuse, E.M. Time-dependent dike propagation from joint inversion of seismicity and deformation data. *J. Geophys. Res.* **118,** 5785–5804 (2013).

10. Felzer, K. R. & Brodsky, E. E. Testing the stress shadow hypothesis. *J. Geophys. Res.* **110,** B05S09 (2005).

11. Mallman, E. P. & Zoback, M. D. Assessing elastic coulomb stress transfer models using seismicity rates in southern California and southwestern Japan. *J. Geophys. Res.* **112,** B03304 (2007).

12. Sigmundsson et al. Segmented lateral dyke growth in a rifting event at Bárðarbunga volcanic system, Iceland. *Nature* **517,** 191–195 (2015).

13. Jakobsdóttir, S. S. Seismicity in Iceland: 1994–2007. *Jökull* **58,** 75–100 (2008)

14. Dieterich, J. A constitutive law for rate of earthquake production and its application to earthquake clustering. *J. Geophys. Res.* **99,** 2601–2618 (1994).

15. Ader, T. J., Lapusta, N., Avouac, J-P. & Ampuero, J-P. Response of rate-and-state seismogenic faults to harmonic shear-stress perturbations. *Geophys. J. Int*. ***198,*** 385–413 (2014).

16. Toda, S., Stein, R. S., Beroza, G. C. & Marsan, D. Aftershocks halted by static stress shadows. *Nat. Geosci.* **5,** 410–413 (2012).

17. Stein, R. S. King, G. C. P . & Lin, J. Change in failure stress on the southern San Andreas Fault system caused by the 1992 Magnitude = 7.4 Landers Earthquake. *Science* **258,** 1328–1332 (1992).

18. Dieterich, J. H., Cayol, V. & Okubo, P. The use of earthquake rate changes as a stress meter at Kilauea Volcano. *Nature **408,*** 457–460 (2000).

19. Toda, S., Stein, R. S. & Sagiya, T. Evidence from the AD 2000 Izu islands earthquake swarm that stressing rate governs seismicity. *Nature **419,*** 58–61 (2002).

20. Segall, P., Desmarais, E. K., Shelly, D., Miklius, A. & Cervelli, P. Earthquakes triggered by silent slip events on Kilauea volcano, Hawaii. *Nature **442,*** 71–74 (2006).

21. Lohman, R. B. & McGuire, J. J. Earthquake swarms driven by aseismic creep in the Salton Trough, California. *J. Geophys. Res.* **112,** *B04405* (2007).

Online Methods:
Earthquake Location
We use the Coalescence Microseismic Mapping (CMM) technique[31] to automatically detect and locate seismic events recorded during the dyke intrusion. The CMM computer program calculates the ratio between the average amplitude in a short term and a long term window along the seismic trace. Peaks in this function at each receiver are then migrated into a 3D subsurface travel time grid, computing a coalescence function through time at each grid point. Peaks in the coalescence function define earthquake locations and origin times which best fit both the P and S-wave seismic energy arriving at all the receivers. Using our long running and dense local seismic network (see Supplementary Figure 9 for the network coverage) we construct a self-consistent seismicity catalogue of over 30,000 earthquakes from before the crisis began through to 3rd September 2014, shortly after the fissure eruption started.

Over 200 triggered earthquakes were refined by manually picking P and S-wave arrival times and polarities and located using NonLinLoc, a probabilistic non-linear earthquake location program[32]. A 1D linear gradient velocity model (Supplementary Figure 10 & Table 3) derived from the ICEMELT refraction experiment[33] was used to locate events. In this model we use a constant Vp/Vs ratio of 1.78 calculated from Wadati plots[34]. The events were then relocated using HypoDD[35] to reduce the effect of seismic velocity heterogeneity. The layered velocity model required by HypoDD was generated by an approximation to the

gradient model used in NonLinLoc. This tightened the hypocentral locations and clearly delineated faults. Ray take-off angles from the absolute event locations were then used to generate first motion polarity fault-plane solutions[36]. An average of 40 polarity picks were used to constrain fault-plane solutions, but only events with complete and tight coverage of the focal sphere were retained in the swarm analysis. Representative focal mechanisms for each swarm were found by averaging the most consistent mechanisms, and where a consistent fault plane was not evident the nodal plane best aligned to the pervasive rift fabric was selected. A complete hypocentre and focal mechanism list is provided in the Supplementary Information.

Geodetic Inversion

We use daily GPS solutions[12] and the earthquake locations to invert for the amount of opening on each segment of the dyke during each 24 hour period. The geometry of nine dyke segments is defined by the location of the earthquakes and only the segments which are seismically active on any particular day were allowed to open during the inversion.

As dyke seismicity is likely to be controlled by stress concentrations near the base of the intrusion[9], we assume that the bottoms of our dyke segments are near the average depth of the earthquakes. Because of the far-field location of the GPS stations, the geodetic data is mainly sensitive to the volume of the intrusion rather than its precise geometry. Because of this, a trade-off exists between the amount of opening and the vertical extent of the dyke. Therefore, we assume that the top of the dyke is at a fixed depth of 2 km below sea level, but shallows near the eruption site. The choice of the depth to the top of the dyke only affects the absolute size of the induced stresses and so does not influence our overall result of the timing and spatial variation of coulomb stress.

The total GPS displacements at all available stations from the intrusion period are then used to constrain the depth and location of a deflation source beneath Bárðarbunga caldera that fits the data, along with our best dyke opening model. The best result from a grid search over depth, location, size and contraction of the source is a horizontal sill beneath the centre of Bárðarbunga caldera (star on Figure 3) at 16.8 km depth below sea level. The constraint of this is shown in Supplementary Figure 1.

Having fixed the geometry of the dyke and the deflation source, we then construct a time dependent

model of the deformation. On each day we use the observed cumulative GPS displacement from campaign and continuous GPS stations to invert for both the opening of the active dyke segments and the deflation at Bárðarbunga. Opening on any segment that is no longer active remains fixed. The inversion is performed using a Nelder-Mead Simplex function to minimise the misfit between the observed GPS displacements and those calculated assuming an elastic half space[37] with Coulomb3.3 routines[38,39]. We use a Young's modulus of 45 GPa and a Poisson's ratio of 0.25 as calculated by Auriac et al.[40] The coefficient of friction for these areas is not known. We varied it between 0.2 and 0.6 and found it to have little effect on the induced coulomb stress evolution, so it does not alter the main conclusions. All figures (except where specified) were calculated using a coefficient of friction of 0.4. A nearby study of the visco-elastic stress from a dyke intrusion in the Icelandic crust at Upptyppingar[41] found that the viscous stresses were of negligible magnitude compared to the elastic stresses.

Using the time-dependent dyke opening model we calculate the coulomb stress[38,39] field for each cluster on every day. The stresses are calculated using a representative fault at each cluster located at the average depth of the triggered earthquakes: 6 km at Kistufell, 7 km at Kverkfjöll and 6 km at Bárðarbunga (Supplementary Figure 10).

Seismicity – Stressing rate relationships

Dieterich's law for the rate of earthquake production[14] is used to predict seismicity rate changes expected from the coulomb stress function. In such a model there is a short time delay between stress-transfer and earthquake initiation associated with the nucleation process. From this stress-transfer law the predicted seismicity rate can be generated from the stress evolution using the solution for the earthquake rate response to a single discrete stress step. The state variable is evolved in short (hour long) time steps from the interpolated stress function as

$$\gamma(t + \Delta t) = \left(\gamma(t) + \frac{\Delta t}{2A\sigma}\right) exp^{\left(-\frac{S(t+\Delta t)-S(t)}{A\sigma}\right)} + \frac{\Delta t}{2A\sigma}$$

where γ is the state variable, σ is the effective normal stress, A is a fault constitutive parameter and S is the coulomb stress function[42]. The starting state variable is $\gamma(0) = 1/\dot{t}$ where $\dot{t}$ is the background stressing rate. The earthquake rate R at the mid-point of that time step is then

$$R = \frac{r}{\gamma\dot{t}}$$

The seismicity rate is dependent on the known background earthquake rate, r, the background stressing rate, $\dot{t}$, and the product of the effective normal stress and a fault constitutive parameter, $A\sigma$. A parameter sweep of $\dot{t}$ and $A\sigma$ is shown in Supplementary Figure 5, assessed using a simple RMS misfit between predicted and cumulative data. This reveals a trade-off between the parameters, meaning that while the visual fit of the models is good, absolute constraints cannot be placed separately on these values from this study. Best fit parameters at each location (Supplementary Table 2) are used to demonstrate an excellent match between the observed seismicity and seismicity rate changes we would expect from the coulomb stress function (Figures 3 c,f,i).

Data Availability Statement

Full details of the hypocentral locations of the triggered earthquakes and their fault plane solutions are given in electronic supplementary material. Daily GPS positions are from Sigmundsson et al.[12]

Code Availability Statement

Earthquake analysis used freely available software: locations use computer program NonLinLoc[32], double difference relocations used HypoDD[35], and fault plane solutions were generated using FPFIT[36]. Stress modelling used routines from the freely available package Coulomb3.3[38,39].

Methods References:

31. Drew, J., White, R. S., Tilman, F. & Tarasewicz, J., Coalescence Microseismic Mapping. *Geophys. J. Int.* **195,** 1773–1785 (2013).
32. Lomax, A., Virieux, J., Volant, P. & Berge, C. Probabilistic earthquake location in 3D and layered models, in *Advances in Seismic Event Location* (Kluwer, 2000).
33. Darbyshire, F. A., Bjarnason, I. T., White, R. S. & Flovenz, O. Crustal structure above the Iceland mantle plume imaged by the ICEMELT refraction profile. *Geophys. J. Int*. **135,** 1131–1149 (1998)
34. Wadati. K. On the travel time of earthquake waves. *Geophysical Magazine* **7,** 101–111 (1933).
35. Waldhauser, F. & Ellsworth, W. A double-difference earthquake location algorithm: method and application to the northern Hayward fault, California. *Bull. Seismol. Soc. Am.* **90,** 1353–1368 (2000).
36. Reasenberg. P. & Oppenheimer, D. H. FPFIT, FPPLOT, FPPAGE: Fortran computer programs for calculating and displaying earthquake fault-plane solutions. USGS Open-file Report 85–739 (1985).
37. Okada, Y. Internal deformation due to shear and tensile faults in a half-space. *Bull. Seismol. Soc. Am.* **82,** 1018–1040 (1992)
38. Toda, S., Stein, R. S., Richards-Dinger, K. & Bozkurt, S. Forecasting the evolution of seismicity in southern California: Animations built on earthquake stress transfer. *J. Geophys. Res.* **110,** B05S16 (2005).
39. Lin, J. & Stein, R. S. Stress triggering in thrust and subduction earthquakes and stress interaction between the southern San Andreas and nearby thrust and strike-slip faults. *J. Geophys. Res.* **109,** B02303 (2004).
40. Auriac, A., Sigmundsson, F., Hooper, A., Spaans, K. H., Björnsson, H., Pálsson, F., Pinel, V. & Feigl, K. L. InSAR observations and models of crustal deformation due to a glacial surge in Iceland. *Geophys. J. Int*. **198**, 1329–1341 (2014).
41. Martens, H. R. & White, R. S. Triggering of microearthquakes in Iceland by volatiles released from a dyke intrusion. *Geophys. J. Int*. **194,** 1738–1754 (2013).
42. Hainzl, S., Steacy, S. & Marsan, D. Seismicity Models Based on Coulomb Stress Calculations. Community Online Resource for Statistical Seismicity Analysis (2010).

Author Correspondence:

Correspondence and requests for material should be addressed to RGG.

Acknowledgements:

Author Contributions:

All authors participated in data collection from seismometers deployed in Iceland by the Cambridge group, in processing and analysing the seismic data and in interpretation of the results. Geodetic modelling was carried out by T.G. and R.G.G. analysed the seismicity and stressing rates. All authors contributed to preparation of the manuscript.

Competing financial interests statement:

Figure 1 | Earthquake locations showing propagating dyke and resultant seismicity.
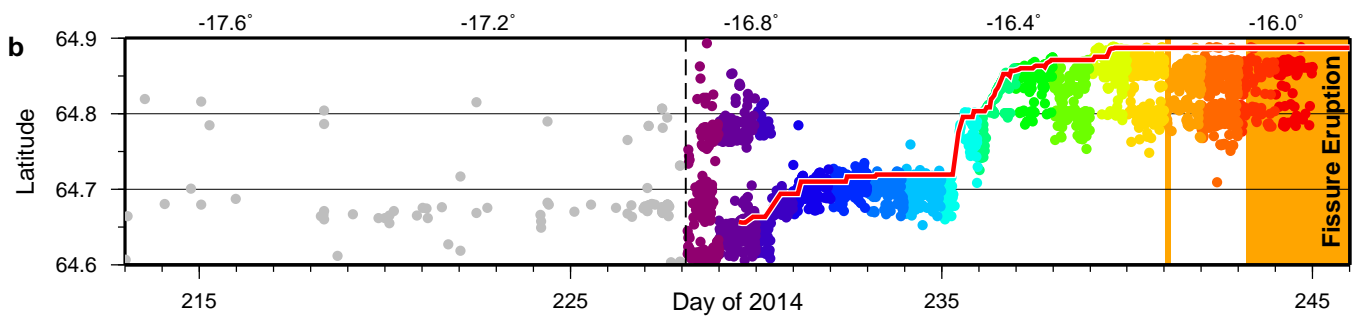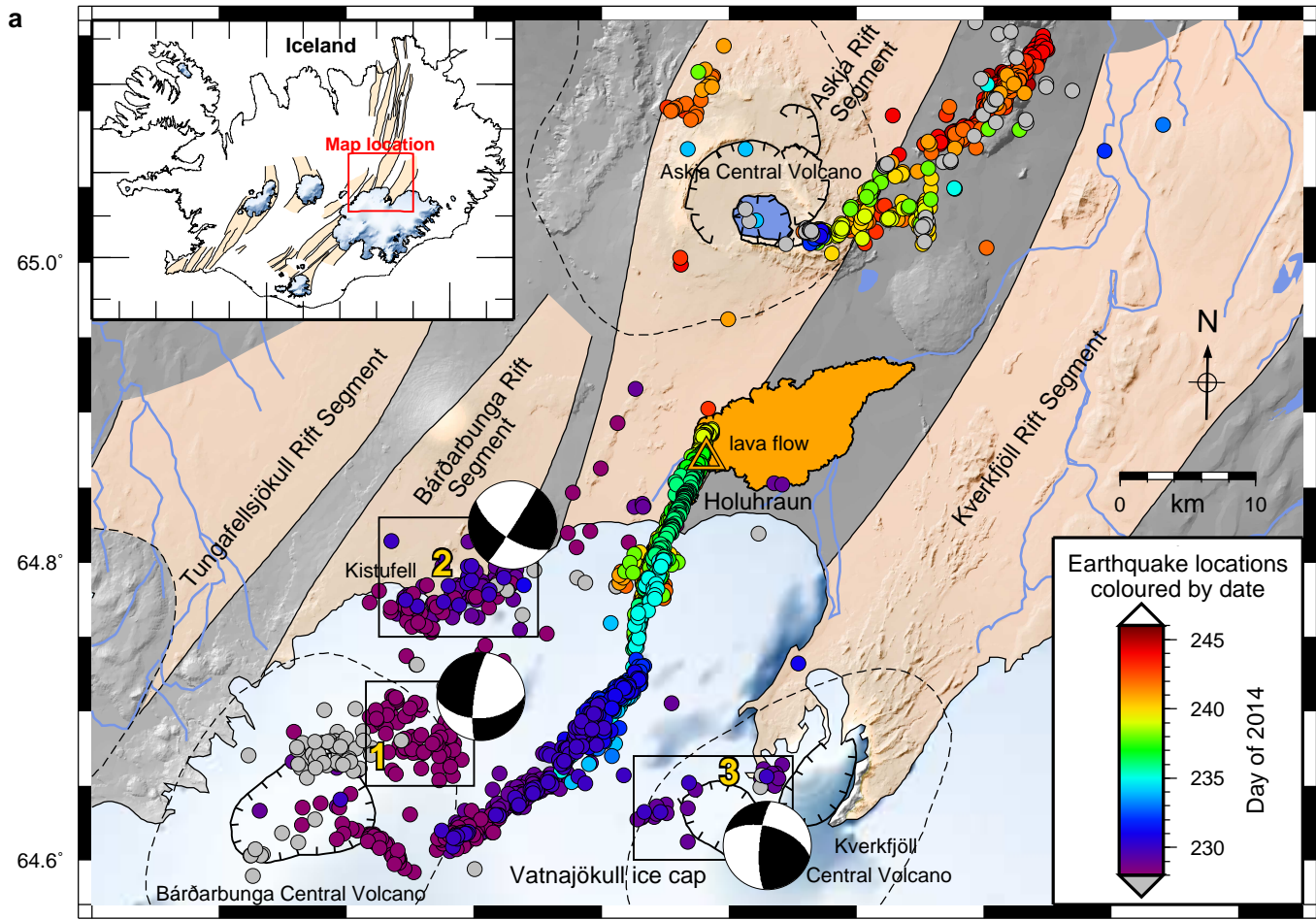
(a) Dots show locations coloured by day of over 30,000 earthquakes generated during the dyke propagation. Grey dots show earthquakes preceding dyke intrusion. See also Supplementary Movie 1. Topography is grey with ice cover in white; beige overlays show rift segments associated with each central volcano (dashed lines). Ticked lines delineate calderas. Triggered regions are marked with labelled boxes and an average fault–plane solution. Orange triangle shows eruption site and orange shading extent of new Holuhraun lava flow. Inset shows map location; (b) propagating dyke tip (red line) along with seismicity rate changes at neighbouring volcanoes.
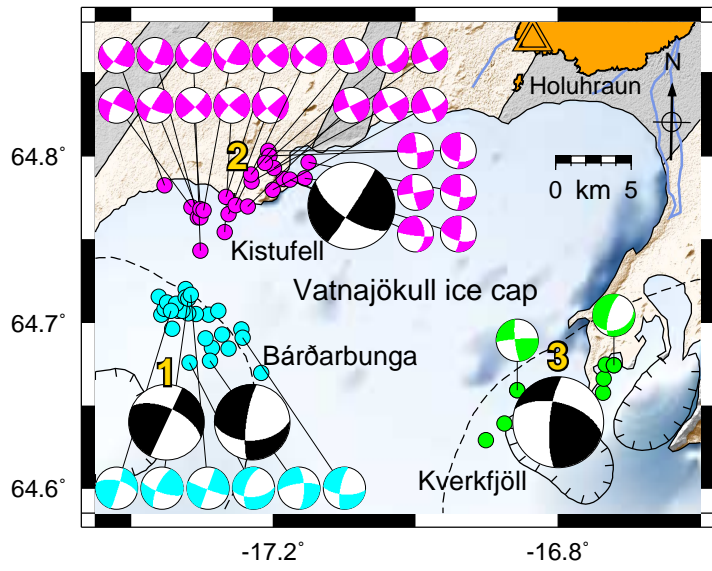
Figure 2 | Manually refined earthquake locations and fault–plane solutions of triggered swarms

Relocated earthquake epicentres shown as coloured dots with fault–plane solutions for each swarm in the Vatnajökull region. Large black fault–plane solutions display the averaged representative focal mechanism for that swarm. Supplementary Figure 12 details Bárðarbunga focal mechanisms. Topography and background as in Figure 1.

Figure 3 | Seismicity activated and suppressed by evolving stress field at three triggered regions (each column).

Daily maps of coulomb stress (red positive, blue negative) on target faults in each region (Figures 1,2). Solid black lines mark ice limit, dashed lines central volcanoes, ticked lines calderas. Green circles highlight earthquakes during the current day, grey circles since dyke onset. Green lines show current dyke geometry. Star is deflation source location. (c,f,i) Red lines show coulomb stress evolution in the target region, blue lines show predicted cumulative seismicity from seismicity–rate equation. Black line is observed cumulative seismicity, grey bars show hourly rates. Dotted line shows stressing rate turning point. Dashed line is time of dyke injection.

a

Iceland

Map location

Askja Rift Segment

Askja Central Volcano

Tungafellsjökull Rift Segment

Bárðarbunga Rift Segment

Kverkfjöll Rift Segment

lava flow

Holuhraun

Kistufell

2

1

3

Bárðarbunga Central Volcano

Vatnajökull ice cap

Kverkfjöll Central Volcano

N

0   km   10

Earthquake locations
coloured by date

245

240

235

230

Day of 2014

65.0°

64.8°

64.6°

b

-17.6°   -17.2°   -16.8°   -16.4°   -16.0°

64.9

64.8

64.7

64.6

Latitude

Fissure Eruption

215   225   235   245

Day of 2014

Bárðarbunga - region 1

a Day 228 noon - Seismicity on

Coulomb Stress/bars
-2 -1 0 1 2

b Day 230 noon - Seismicity off

c Time evolution

Dyke injection

coulomb stress / bar

225   Day of 2014   230

Kistufell - region 2

d Day 229 noon - Seismicity on

e Day 232 noon - Seismicity off

f Time evolution

225   Day of 2014   230

Kverkfjöll - region 3

g Day 230 noon - Seismicity on

h Day 233 noon - Seismicity off

i Time evolution

Cumulative earthquakes

225   Day of 2014   230